Lasers in Manufacturing Conference 2025

Ultrashort Pulse Laser-assisted Sample Preparation for High-resolution X-ray Microscopy

Hardik Vaghasiya[a], Murilo Izidoro Santos[b], Hoang Thinh Nguyen[b] , Paul Miclea,[c,a,b,1]

[a]*ZIK Sili-Nano,MLU Halle-Wittenberg, Karl-Freiherr-von-Fritsch-Straße 3, 06120 Halle (Saale), Germany*
[b]*Fachgruppe µMD, MLU Halle-Wittenberg, Heinrich-Damerow- Straße, 06120 Halle (Saale), Germany*
[c]*Fraunhofer Center for Silicon Photovoltaics CSP, Otto-Eissfeldt- Straße 12, 06120 Halle (Saale), Germany*

Abstract

X-ray microscopy (XRM) is revolutionizing materials development, exploration, and failure analysis due to its non-destructive imaging and high resolution down to 50 nm. However, preparing cylindrical XRM samples with several tens of microns diameters poses significant challenges. Traditional methods like Focused Ion Beam (FIB) have mainly been used, which are precise but extremely time-consuming and unsuitable for high throughput. Addressing this issue, this study explores the application of femtosecond laser ablation in XRM sample preparation, emphasizing its advantages in achieving smooth, defect-free surfaces and precise material removal. Experimental results demonstrate the ability of femtosecond lasers to produce well-defined sample geometries, even in challenging materials such as metals, semiconductors, dielectrics and polymers, facilitating more accurate XRM measurements. Our findings underline the potential of femtosecond laser technology as a reliable, efficient, and versatile tool for enhancing XRM sample preparation workflows, paving the way for improved material characterization and advanced structural analysis.

Keywords: Femtosecond laser ablation, X-ray microscopy (XRM) ; X-ray microCT; Laser micromachining

1. Introduction

X-ray microscopy (XRM) at the nanometer scale, also named nano-computed tomography (nano-CT), has revolutionized three-dimensional microstructural analysis, enabling non-destructive imaging with resolutions approaching tens of nanometers (Vásárhelyi *et al.*, 2020; Vogtmann *et al.*, 2021; Villarraga-Gómez *et al.*, 2022). This imaging modality is increasingly used in materials science, microelectronics, energy systems, and biomedical research, where quantitative internal structure visualization is essential (Liss *et al.*, 2003; Sedigh Rahimabadi, Khodaei and Koswattage, 2020). A critical constraint in nano-CT is sample geometry (Bailey *et al.*, 2017). For optimal tomographic reconstructions of electron-dense materials, samples must be prepared as small cylindrical pillars (typically 20–100 µm in diameter) with rotational symmetry. Improper geometry can lead to artifacts in reconstruction, underutilization of field-of-view (FOV), and beam-hardening effects, particularly for high-density materials (Bailey *et al.*, 2017; Hubler, Gelb and Ulm, 2017). Therefore, reliable and reproducible preparation of samples with the desired size and shape is essential for maximizing imaging performance.

Conventional methods such as focused ion beam (FIB) milling or plasma FIB (PFIB) are capable of producing such geometries with high accuracy (Pang and Xu, 2023; Tang *et al.*, 2024). However, they are notoriously time-intensive, often requiring several hours to days per sample, and present challenges in throughput, cost, and material compatibility. Mechanical methods, while faster, lack the resolution and flexibility to shape complex or small-volume specimens (Ditscherlein, Leißner and Peuker, 2022). Thus, there is a clear need for a rapid, precise, and material-flexible alternative to conventional

* Corresponding author. Tel.:+49 0345 895413.
E-mail address: paul-tiberiu.miclea@physik.uni-halle.de.

preparation workflows. To address these constraints, ultrashort pulse (USP) laser micromachining has emerged as a powerful alternative. Due to their extremely short pulse durations, femtosecond lasers enable "cold ablation," minimizing thermal damage and eliminating heat-affected zones (HAZ) (Vaghasiya et al., 2022). This makes them well suited for preparing samples in polymers, semiconductors, dielectrics, and composites (Bliedtner *et al.*, 2016; Malinauskas *et al.*, 2016). Compared to FIB, laser micromachining offers six orders of magnitude higher ablation rates and enables the production of sample-ready geometries in minutes rather than days (Tordoff *et al.*, 2020).

The primary focus of this work is to develop and optimize a USP laser-based method for fabricating high-quality cylindrical samples suitable for nano-CT analysis. This approach aims to balance fast material removal with precise dimensional control and minimal thermal damage. Femtosecond laser ablation is used to produce rotationally symmetric micro-pillars with smooth surfaces and minimal taper for accurate tomographic imaging. By tailoring laser process parameters for different materials such as silicon, titanium dioxide, and graphite–polymer composites, this method demonstrates broad applicability and efficiency. Validation has been established through nano-CT, confirming the suitability of the prepared samples for advanced 3D imaging applications.

2. Experimental

2.1 Material

To evaluate the applicability and robustness of the laser-assisted sample preparation approach, three distinct classes of materials were selected: silicon, titanium dioxide (TiO_2), and a graphite–polymer composite. These materials were chosen to represent a range of physical and structural properties commonly encountered in materials science and X-ray microscopy applications. Silicon was used as a representative semiconductor material due to its widespread use in microelectronics and its well-characterized structural uniformity. It serves as a benchmark for testing precision and structural integrity during micromachining. Titanium dioxide, a typical ceramic material, was selected for its hardness and brittleness, which make it challenging to process using conventional methods. It provided a test case for assessing the technique's ability to maintain structural quality in materials that are prone to cracking or chipping. The third material, a composite consisting of 80% graphite and 20% polypropylene, introduced a heterogeneous and relatively soft system into the study. This material was selected to test the method's performance on multi-phase samples, particularly in managing different ablation behaviors and avoiding surface artifacts.

2.2 *Laser System Configuration*

All experiments were carried out using a femtosecond laser system equipped with galvanometric scanning optics. The system operated at a wavelength of 515 nm with a pulse duration of 180 femtoseconds. The laser beam had a Gaussian profile, and the spot diameter at the focus ranged between 10 and 20 micrometers, depending on the process. The repetition rate was adjustable for each process step to match the ablation needs of different materials. The lase fluence was tuned according to the material properties and the specific stage of the structuring process. The galvanometric setup enabled precise and rapid beam movement, while fine control over pulse overlap and scanning speed allowed optimization for various geometries and material responses.

2.3 Nano-Computed Tomography (Nano-CT) Imaging

Samples were imaged using a Zeiss Xradia Ultra 810 X-ray microscope equipped with a Zernike phase ring for phase-contrast imaging of low-density materials. To ensure mechanical stability and precise alignment during rotational tomography, samples were mounted on custom pin holders featuring v-shaped kerfs. A small amount of epoxide adhesive was applied to the v-kerf surfaces prior to mounting to secure the samples in place. Pins containing the samples were transferred to the sample stage in the equipment and 1001 projection images were acquired on large field of view mode (FOV size: 64 µm x 64 µm) over 180°, using an exposure time of 50 s. Titanium dioxide (TiO_2) sample were imaged on absorption contrast mode, leveraging a binning 1 pixel count on the detector. Graphite-polymer composites were imaged on phase-contrast mode, leveraging a binning 2 for increased intensity throughput. The resulting datasets were processed and reconstructed using Zeiss proprietary software (XMReconstructor).

2.4 Image processing and dataset rendering

Reconstructed datasets of titanium-based samples were processed using Avizo 9.7.0 (Thermo Fisher Scientific). Datasets were filtered using a non-local means-based algorithm, then, the titanium particles were segmented based on the grayscale intensities of the images (Interactive thresholding), and 3D rendered. Reconstructed datasets of graphite composites were processed in Dragonfly 3D (Object Research Systems), using a U-Net based AI-segmentation tool to segment the graphite phase. The segmented datasets were further used for phase quantification and mesh generation. In selected cases, the datasets were also used as input for computational simulations of in-plane conductivity using the formation factor experiment simulation embedded in the Avizo XLab Suite.

3. Results and Discussion

3.1 Sample Preparation Workflow

The core objective of this work was to establish a robust, repeatable, and material-independent workflow for preparing cylindrical samples suitable for nano-CT. To achieve this, a four-step ultrashort pulse (USP) laser structuring process was developed. This approach focused on optimizing both the geometry and surface quality of the samples, while maintaining compatibility with imaging systems that require rotation symmetry and minimal sample artifacts. Each step in the workflow was designed to accommodate material-specific responses to laser ablation while ensuring efficiency and precision. The full workflow is illustrated in Figure 1. It includes trench milling, undercutting, pillar formation, and breaking point finalization.

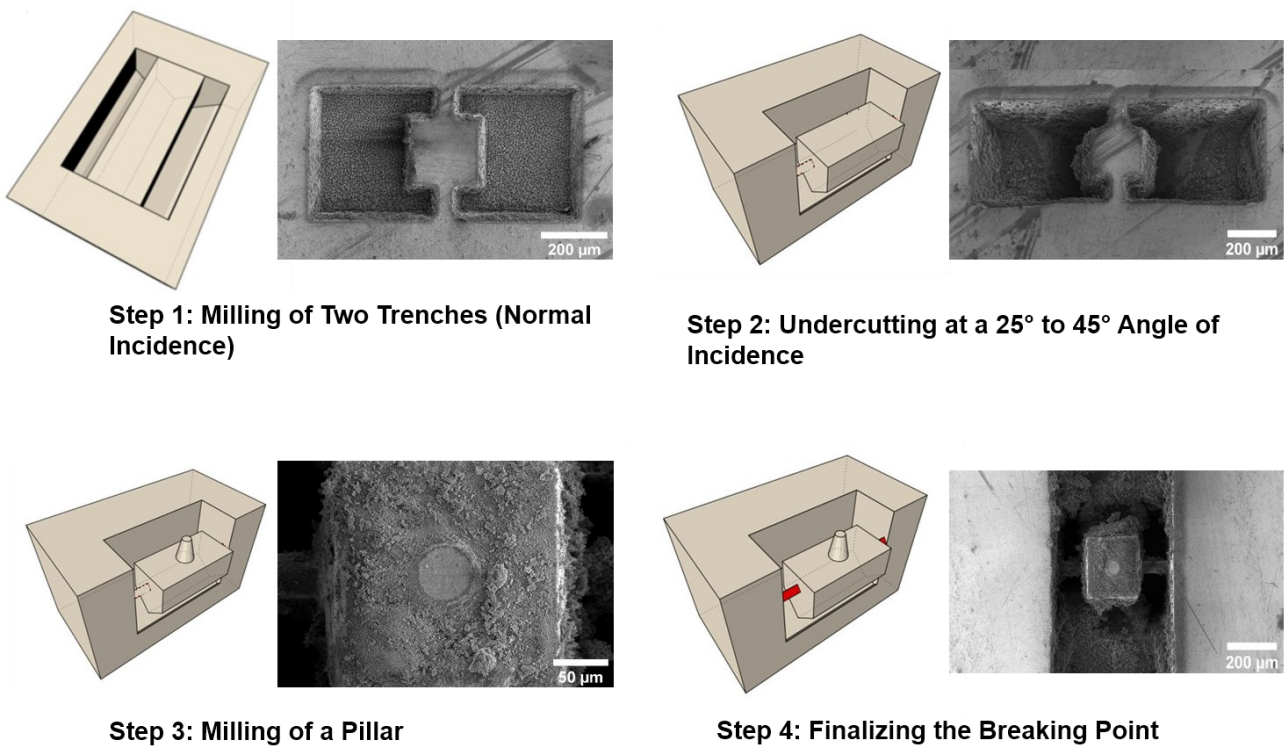

Figure 1 Nano-CT sample preparation workflow. CAD rendering adapted from (Krause *et al.*, 2023)).

The first step involved **trench milling** under normal laser incidence. Two parallel trenches were ablated into the surface of the sample, outlining the lateral boundaries of the cylindrical region to be isolated. This step was critical for defining the pillar geometry and ensuring dimensional symmetry. This step ensured that the final sample would have a uniform cross-section and symmetrical geometry suitable for 360° rotational imaging.

The second step involved **undercutting**, which played a critical role in preparing the base of the sample for mounting. Using angled laser incidence, typically in between 25° and 45°, material beneath the target pillar was ablated to form a tapered

base. This geometry was specifically designed to match the V-shaped kerf in the customized sample pins used for XRM mounting. The V-shaped kerf provides mechanical support and alignment, allowing the sample to remain centered and stable during tomographic rotation. Undercutting not only aids in detaching the sample from the bulk but also guarantees compatibility with the pin mount, ensuring minimal vibration or misalignment during scanning. Special care was taken during this step to prevent over-ablation, which could weaken the structure or introduce instability.

The third step was **pillar formation**, which completed the shaping of the cylindrical sample. This was achieved using bi-directional raster scanning across the pre-trenched region, gradually removing material to refine the diameter and height of the pillar. This step involved structured ablation within the region defined by the trenches to sculpt the final cylindrical pillar. Throughout this step, careful control over energy delivery was necessary to avoid excessive ablation at the edges or the formation of heat-affected zones. The final pillar dimensions typically ranged from 20 to 80 µm in diameter and approximately 300 µm in height. The resulting structures showed minimal taper and no visible conicity, ensuring proper alignment in tomographic systems.

The final step, **breaking point finalization**, was designed to facilitate clean and controlled detachment of the pillar from the bulk material. A localized weakening was introduced near the base of the pillar, usually at the narrowest point formed by the undercut. This was accomplished using low laser power and minimal repetition to reduce material thickness without compromising the rest of the structure. The purpose of this step was to allow the sample to be gently removed using precision tweezers, avoiding mechanical stress that might lead to fracture or deformation. Successful detachment required minimal force, and most samples could be lifted directly from the kerf and transferred to the imaging stage without additional preparation.

3.2 Material-Specific Results

The laser-based sample preparation workflow was applied to three material systems: monocrystalline silicon, titanium dioxide (TiO_2), and a graphite–polymer composite (80/20 by weight). Each material required adjustments in laser parameters due to differences in thermal conductivity, absorption characteristics, and mechanical behavior. A summary of all laser process parameters for each material and step is provided in Table 1.

Table 1. Laser Processing Parameters for XRM Sample Preparation

Material	**Step**	**Power (W)**	**Spot Size (mm)**	**Repetitions**	**Scan Pattern**
Silicon	Trench Milling	0.320	0.015	3	Bi-directional
	Undercutting	0.400	0.010	3	Bi-directional
	Pillar Formation	0.400	0.010	10	Bi-directional
	Breaking Point	0.250	0.015	2	Crisscross
Titanium Dioxide (TiO_2)	Trench Milling	0.250	0.015	2	Bi-directional
	Undercutting	0.300	0.010	3	Bi-directional
	Pillar Formation	0.400	0.010	12	Bi-directional
	Breaking Point	0.150	0.010	1	Crisscross
Graphite–Polymer (80/20)	Trench Milling	0.300	0.015	3	Bi-directional
	Undercutting	0.300	0.010	6	Bi-directional
	Pillar Formation	0.300	0.010	10	Bi-directional
	Breaking Point	0.250	0.015	2	Crisscross

Silicon exhibited stable and repeatable ablation characteristics under ultrashort pulse laser structuring. Clean trenches and consistent pillar shapes were achieved across multiple samples. The trench milling and pillar formation stages produced straight, vertical sidewalls with negligible taper. Undercutting was successful at angle of 45°, resulting in a smooth transition to the V-shaped kerf support geometry. No delamination, chipping, or microcracking was observed under SEM inspection. The breaking point was clearly localized and allowed for clean detachment without mechanical deformation. The final samples demonstrated both dimensional precision and mechanical robustness required for XRM imaging.

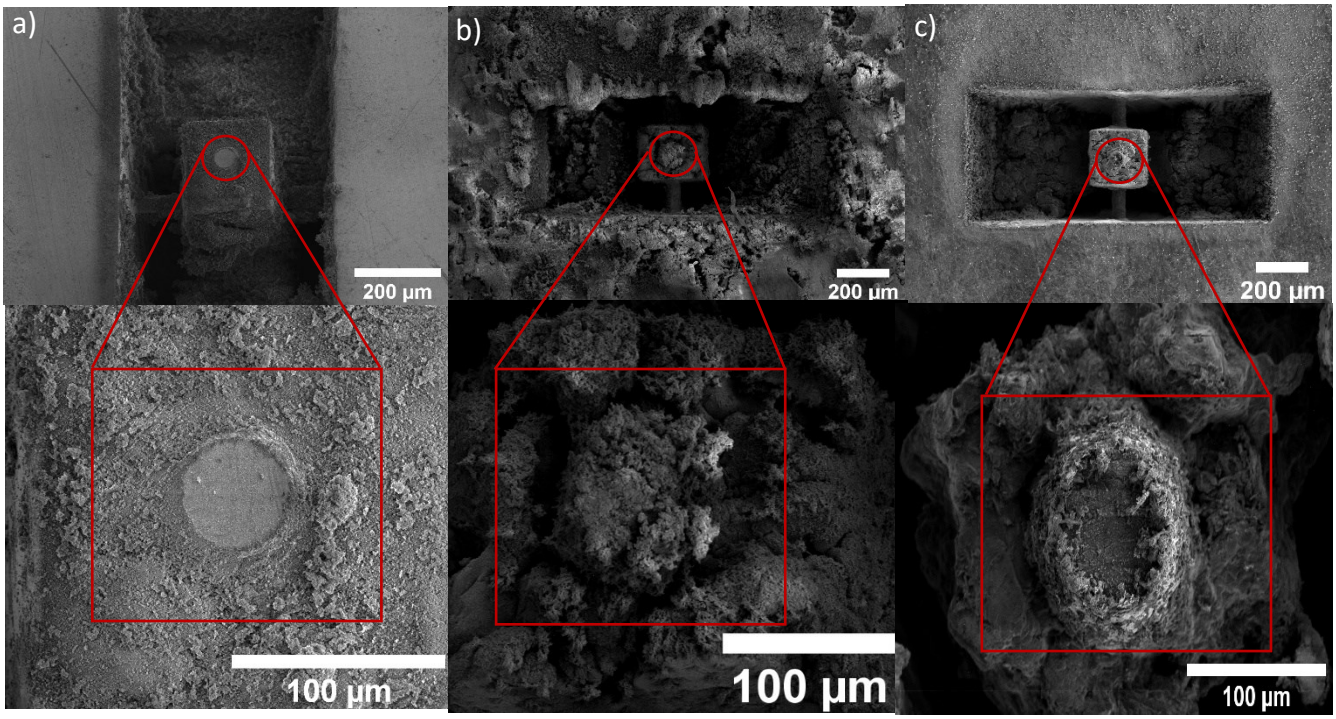

Figure 2 SEM images of laser-fabricated cylindrical samples prepared using the ultrashort pulse laser structuring workflow. a) Silicon, b) Titanium dioxide (TiO_2) and c) Graphite–polymer composite.

Titanium dioxide is a brittle ceramic which posed more significant challenges due to its low thermal conductivity and higher susceptibility to cracking. To accommodate this, laser power and repetition rates were reduced during trench milling and undercutting. The undercut angle was limited to 35° to avoid excess material removal near the base. SEM images of the fabricated TiO_2 sample are shown in Figure 2 b). The trench geometry is well defined, with a centrally positioned pillar and visible undercut. Although surface debris from redeposition is present, the core structure remains intact. The pillar maintains its intended shape, and the undercut profile aligns with the V-shaped kerf mount, confirming the process's mechanical alignment strategy. No fractures, delamination, or deformation were observed. The observed surface roughness is attributed to partial melting and re-solidification of fine ceramic particles, which did not impact the structural or imaging performance of the pillar.

The graphite–polymer composite required further tuning due to its heterogeneous nature. The polymer and graphite phases exhibit different ablation thresholds, causing uneven energy coupling if not properly managed. Additional repetitions and increased scan overlap were introduced, particularly in the undercutting and pillar formation steps, to ensure uniform removal. SEM analysis revealed that while the pillar sidewalls were less smooth than those of silicon. The overall geometry remained consistent and centered. No structural delamination occurred, and the breaking point was successfully localized for manual detachment. Surface texture was rougher due to the composite's internal inhomogeneity, but the cylindrical shape and structural integrity were preserved.

3.3 Nano-CT Imaging

Selected samples were imaged using nano-CT to evaluate their internal structure, geometric consistency, and phase distinguishability after laser preparation. The TiO_2 and graphite–polymer composite samples were chosen because of the different class of materials. The resulting volumetric data were segmented and analyzed using grayscale intensity thresholds and surface rendering techniques to assess structure and imaging compatibility.

3.3.1 Titanium Dioxide (TiO_2)

To evaluate the internal structure and geometric quality of the laser-prepared TiO_2 sample, 3D nano-CT was performed using absorption contrast mode. The resulting volume was rendered along the three principal axes (X, Y, and Z) to assess the consistency of the pillar geometry, surface characteristics, and potential internal artifacts. Figure 3 shows the surface renderings from each viewing direction. The X-axis rendering (Figure 3 a), left) provides an oblique view that captures the taper of the cylindrical pillar, as well as the curvature and clean separation from the trench. The outer surface appears smooth with visible ablation striations from the raster scanning process. Debris from laser processing is present near the top and side regions, but it remains external to the sample structure. In the Y-axis view (Figure 3 b), center), the pillar is visualized orthogonally along its vertical axis. The side profile confirms that the sample maintains structural symmetry and consistent diameter. Surface-level debris and ablation byproducts are more apparent in this orientation, particularly around the upper surface, but the core remains solid. No cracks or structural discontinuities are observed. The Z-axis rendering (Figure 3 c), right) offers a view perpendicular to the sample base. This view highlights the successful taper formed by the undercutting step, which enables secure placement in a V-groove mount. A single subsurface cavity is visible near the base of the pillar. This void may result from localized over-ablation or pre-existing porosity in the bulk material. However, the rest of the structure appears dense and continuous, and the cavity is spatially isolated.

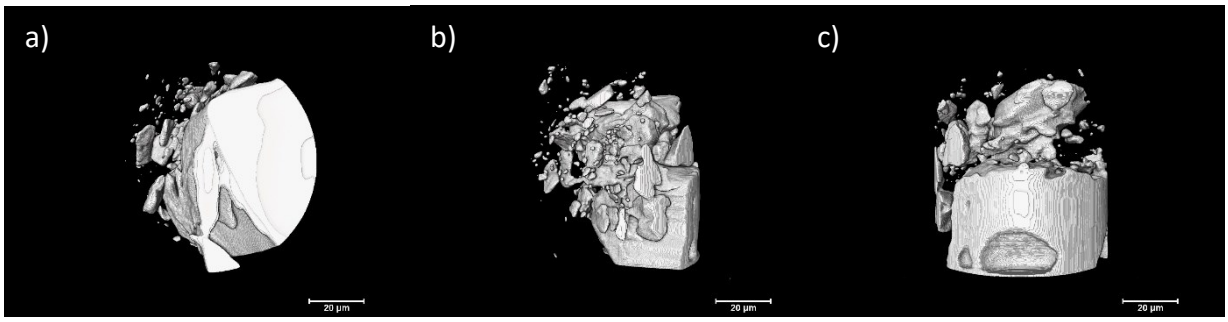

Figure 3 3D nano-CT renderings of the TiO_2 sample along, a) X-axis, b) Y-axis, and, c) Z-axis.

3.2.2 Graphite–Polymer Composite

X-ray microscopy of the graphite–polymer composite revealed detailed insights into its heterogeneous internal structure. The material, composed of 80% graphite and 20% polypropylene, was imaged using Zernike phase contrast due to the small difference in the X-ray absorption between the two components.

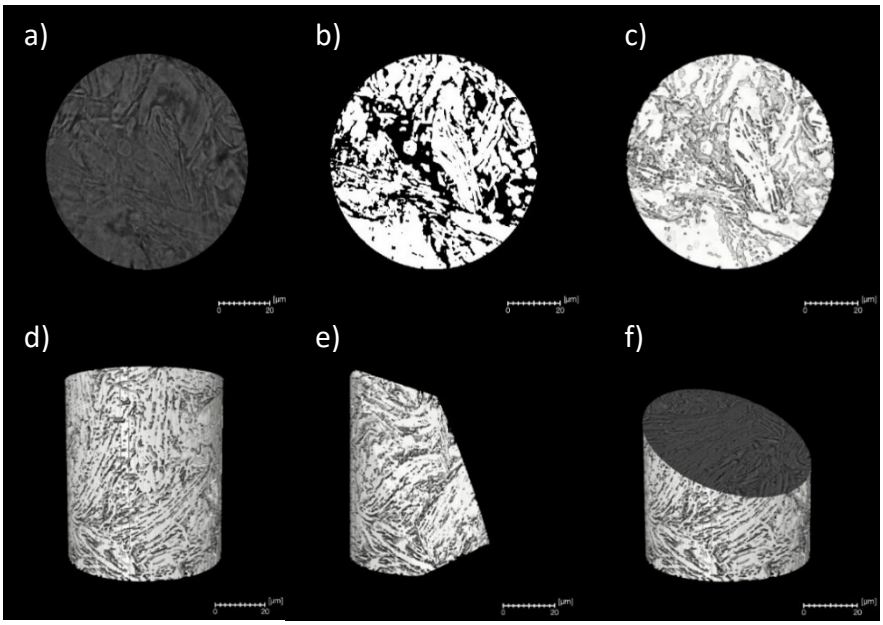

Figure 4 Nano-CT and segmentation results for the graphite–polymer composite sample. Top row (left to right): a) Virtual slice showing grayscale contrast between graphite (bright) and polymer (dark), b) Binary segmentation of the graphite phase (white), and c) Phase-labeled rendering highlighting spatial distribution of graphite flakes. Bottom row (left to right): (d–f) 3D volume renderings of the segmented graphite phase from multiple viewing angles, demonstrating structural continuity and internal connectivity.

The grayscale reconstructions enabled visualization of the graphite particles due to the edge-enhancing effect of the phase-contrast imaging (Figure 4 a)), and highlighted the irregular, flake-like distribution of graphite particles embedded within the polymer matrix. Due to the challenging segmentation of phase-contrast imaged datasets, the graphite phase was segmented from the surrounding polymer using an AI-assisted segmentation method (Figure 4 b)), where the graphite phase is shown in white. To assess spatial continuity, a 3D rendering of the segmented graphite network was generated (Figure 4 d-f)). The resulting volume demonstrates a highly interconnected structure, with graphite domains forming a percolating network through the cylindrical pillar. The surface appears rougher compared to monolithic materials like TiO_2, but the core structure remained stable during rotation and reconstruction.

Following segmentation of the graphite phase, the 3D dataset was imported into post-processing environments for further analysis. Figure 5 a) shows a thickness and density map of the polymer phase, generated using Dragonfly software. Local variations in polymer thickness, ranging from 0.5 to 4.6 µm, are clearly resolved. These spatial thickness distributions can inform mechanical modeling or assess potential weak points in the composite matrix. In parallel, the segmented graphite network was analyzed using Avizo XLab to perform a simulation of electrical conductivity based on the real 3D microstructure (Figure 5 b)). The color-coded conductivity map reveals the spatial distribution of current pathways through the graphite phase, where regions of higher local connectivity exhibit stronger conduction. This type of simulation is particularly valuable for evaluating the percolation behavior and anisotropic properties of conductive composites. The method provides critical insights into phase connectivity and filler distribution, supporting the optimization of composite designs for bipolar plate and other energy-related applications.

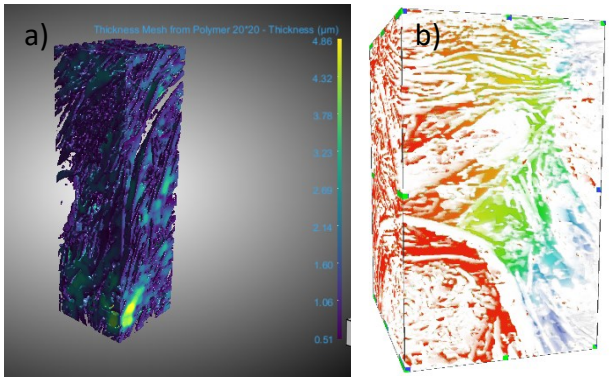

Figure 5 Nano-CT-based structural analysis and simulation of the graphite–polymer composite. a) Thickness map of the polymer phase, and b) Electrical conductivity simulation based on the segmented graphite network.

4. Conclusion

This study demonstrated the successful application of femtosecond laser structuring as a reliable and versatile method for preparing samples for nano-computed tomography (nano-CT). The developed workflow enabled the fabrication of cylindrical pillars from diverse material classes, including ceramics (TiO_2), semiconductors (Si), and composite materials (graphite–polymer), each mounted precisely using a V-groove trench strategy. The laser ablation process produced smooth, crack-free surfaces with precise geometry, suitable for non-destructive imaging. Nano-CT imaging of the TiO_2 sample confirmed structural integrity and uniform internal contrast, with only minor defects such as localized cavities detected. The graphite–polymer composite was imaged leveraging Zernike phase-contrast, enabling successful segmentation using an AI-assisted method. The segmented graphite phase was 3D rendered, revealing details on the graphite particle distribution and on matrix interfaces. In summary, the results confirm that ultrashort pulse laser preparation is not only compatible with advanced imaging techniques but also enhances the throughput and quality of sample preparation. The integration of imaging and simulation workflows provides a powerful foundation for future studies in materials development, composite optimization, and microstructural analysis.

Acknowledgements

The authors gratefully acknowledge the funding and support provided by the WIR!–GRAVOmer-SmartGlass-UKP project (Grant No. 03WIR2015A).

References

Bailey, J.J. *et al.* (2017) 'Laser-preparation of geometrically optimised samples for X-ray nano-CT', *Journal of Microscopy*, 267(3), pp. 384–396. Available at: https://doi.org/10.1111/jmi.12577.

Bliedtner, J. *et al.* (2016) 'Ultrashort Pulse Laser Material Processing', *Laser Technik Journal*, 13(5), pp. 46–50. Available at: https://doi.org/10.1002/latj.201600037.

Ditscherlein, R., Leißner, T. and Peuker, U.A. (2022) 'Preparation strategy for statistically significant micrometer-sized particle systems suitable for correlative 3D imaging workflows on the example of X-ray microtomography', *Powder Technology*, 395, pp. 235–242. Available at: https://doi.org/10.1016/j.powtec.2021.09.038.

Hubler, M.H., Gelb, J. and Ulm, F.-J. (2017) 'Microtexture Analysis of Gas Shale by XRM Imaging', *Journal of Nanomechanics and Micromechanics*, 7(3). Available at: https://doi.org/10.1061/(asce)nm.2153-5477.0000123.

Krause, M. *et al.* (2023) 'Laser-based sample preparation for high-resolution X-ray-computed tomography of glasses and glass ceramics', *Journal of Microscopy*, 289(1), pp. 20–31. Available at: https://doi.org/10.1111/jmi.13147.

Liss, K.-D. *et al.* (2003) 'High-Energy X-Rays: A tool for Advanced Bulk Investigations in Materials Science and Physics', *Texture, Stress, and Microstructure*, 35(3–4), pp. 219–252. Available at: https://doi.org/10.1080/07303300310001634952.

Malinauskas, M. *et al.* (2016) 'Ultrafast laser processing of materials: From science to industry', *Light: Science and Applications*. Nature Publishing Group. Available at: https://doi.org/10.1038/lsa.2016.133.

Pang, S. and Xu, C.S. (2023) 'Methods of enhanced FIB-SEM sample preparation and image acquisition', in *Methods in Cell Biology*. Academic Press Inc., pp. 269–300. Available at: https://doi.org/10.1016/bs.mcb.2023.01.019.

Sedigh Rahimabadi, P., Khodaei, M. and Koswattage, K.R. (2020) 'Review on applications of synchrotron-based X-ray techniques in materials characterization', *X-Ray Spectrometry*. John Wiley and Sons Ltd, pp. 348–373. Available at: https://doi.org/10.1002/xrs.3141.

Tang, T. *et al.* (2024) 'Characterization of human trabecular bone across multiple length scales using a correlative approach combining X-ray tomography with LaserFIB and plasma FIB-SEM', *Scientific Reports*, 14(1). Available at: https://doi.org/10.1038/s41598-024-72739-8.

Tordoff, B. *et al.* (2020) 'The LaserFIB: new application opportunities combining a high-performance FIB-SEM with femtosecond laser processing in an integrated second chamber', *Applied Microscopy*. Springer. Available at: https://doi.org/10.1186/s42649-020-00044-5.

Vaghasiya, H., Krause, S. and Miclea, P.T. (2022) 'Thermal and non-thermal ablation mechanisms in crystalline silicon by femtosecond laser pulses: Classical approach of the carrier density two temperature model', *Journal of Physics D: Applied Physics*, 55(17). Available at: https://doi.org/10.1088/1361-6463/ac4dca.

Vásárhelyi, L. *et al.* (2020) 'Microcomputed tomography–based characterization of advanced materials: a review', *Materials Today Advances*. Elsevier Ltd. Available at: https://doi.org/10.1016/j.mtadv.2020.100084.

Villarraga-Gómez, H. *et al.* (2022) 'Improving the dimensional accuracy of 3D x-ray microscopy data', *Measurement Science and Technology*, 33(7). Available at: https://doi.org/10.1088/1361-6501/ac5a30.

Vogtmann, J. *et al.* (2021) '3d x-ray microscopy as a tool for in depth analysis of the interfacial interaction between a single carbon fiber and an epoxy matrix after mechanical loading', *Journal of Composites Science*. MDPI AG. Available at: https://doi.org/10.3390/jcs5050121.